Magnetotransport and *ab initio* calculation studies on the layered semimetal $CaAl_2Si_2$ hosting multiple nontrivial topological states

Hao Su,[1,2,3] Xianbiao Shi,[4,5] Wei Xia,[1,2,3] Hongyuan Wang,[1,2,3] Xuesong Hanli,[1] Zhenhai Yu,[1] Xia Wang,[1,6] Zhiqiang Zou,[1,6] Na Yu,[1,6] Weiwei Zhao,[4,5,*] Gang Xu,[7,†] and Yanfeng Guo[1,8,‡]

[1]*School of Physical Science and Technology, ShanghaiTech University, Shanghai 201210, China*
[2]*Shanghai Institute of Optics and Fine Mechanics, Chinese Academy of Sciences, Shanghai 201800, China*
[3]*University of Chinese Academy of Sciences, Beijing 100049, China*
[4]*State Key Laboratory of Advanced Welding & Joining and Flexible Printed Electronics Technology Center, Harbin Institute of Technology, Shenzhen 518055, China*
[5]*Key Laboratory of Micro-systems and Micro-structures Manufacturing of Ministry of Education, Harbin Institute of Technology, Harbin 150001, China*
[6]*Analytical Instrumentation Center, School of Physical Science and Technology, ShanghaiTech University, Shanghai 201210, China*
[7]*Wuhan National High Magnetic Field Center and School of Physics, Huazhong University of Science and Technology, Wuhan 430074, China*
[8]*CAS Center for Excellence in Superconducting Electronics (CENSE), Chinese Academy of Sciences, Shanghai 200050, People's Republic of China*

(Received 9 November 2019; accepted 29 April 2020; published 21 May 2020)

We report herein the results of magnetotransport measurements and *ab initio* calculations on single crystalline $CaAl_2Si_2$ semimetal. The transport properties could be understood in connection with the two-band model, agreeing well with the theoretical calculations indicating four main sheets of Fermi surface consisting of three hole pockets centered at the Γ point and one electron pocket centered at the *M* point in the Brillouin zone. Magnetotransport measurements showed striking Shubnikov–de Haas oscillations associated with a nontrivial Berry phase, which originate from a hole Fermi pocket indicated by the *ab initio* calculations. The calculations also unveiled that the hole Fermi surface encloses a nodal line setting around the Γ point close to the Fermi level without considering the spin-orbit coupling (SOC). Once the SOC is included, the fragile nodal-line will be gapped and a pair of Dirac points emerge along the high symmetric Γ-*A* direction located at the Brillouin zone coordinates $(0, 0, k_z^D \approx \pm 0.278 \times \frac{2\pi}{c})$, about 1.22 eV below the Fermi level. In addition, the SOC can also induce a topological insulator state along the Γ-*A* direction with a gap of about 3 meV. The results demonstrate $CaAl_2Si_2$ as an excellent platform for the study of novel topological physics with multiple nontrivial topological states.

DOI: 10.1103/PhysRevB.101.205138

I. INTRODUCTION

Topological semimetals (TSMs) have attracted an immense amount of interest because their nontrivial topological band structure could serve as a unique venue for discovering exotic physical properties both in bulk and surface states [1–4], represented by the Dirac fermions [2,5–8], Weyl fermions [1,9–16], Majorana fermions [17,18], and other exotic new fermions beyond Dirac and Weyl fermions [19–23]. The emergence of different topological fermions generally requires protection from specific symmetries and topology of the electronic band structure. For Dirac semimetals (DSMs) with both time-reversal (TR) and space-inversion (SI) symmetries, the fourfold-degenerate Dirac point (DP) formed by two degenerate nodes with opposite chirality also requires the protection of additional symmetry from being annihilated or separated, such as a certain crystalline symmetry [2,6–8]. Once the TR or/and SI is broken, the DP will split into a pair of doubly degenerate Weyl points (WPs), of which the chirality is also symmetry-protected [1,10,14,15]. The realization of Dirac and Weyl fermions in solids has bridged with those predicted in high-energy physics. However, the Lorentz invariance is strictly required in high-energy physics, whereas it is not necessary in solids. When the low-energy excitation breaks the Lorentz invariance, the Dirac/Weyl cones are titled strongly along a certain momentum direction and the DPs and WPs appear on the boundaries between the hole and electron pockets, thus forming the type-II DSM and Weyl semimetal (WSM) [24–27]. The peculiar band topology in the type-II family can produce many exotic phenomena, such as Klein tunneling in momentum space [28], anisotropic electric transport [29], angle-dependent chiral anomaly [30], etc.

Regarding the various nontrivial topological states, it is natural to question whether one can combine different topological states into a single material in order to produce multiple functionalities from the well-separated nontrivial topological states, or the interplay among them. However, due to the different symmetry requirements, the simultaneous realization of different topological states in a single material

*Author to whom all correspondence should be addressed: wzhao@hit.edu.cn
†gangxu@hust.edu.cn
‡guoyf@shanghaitech.edu.cn

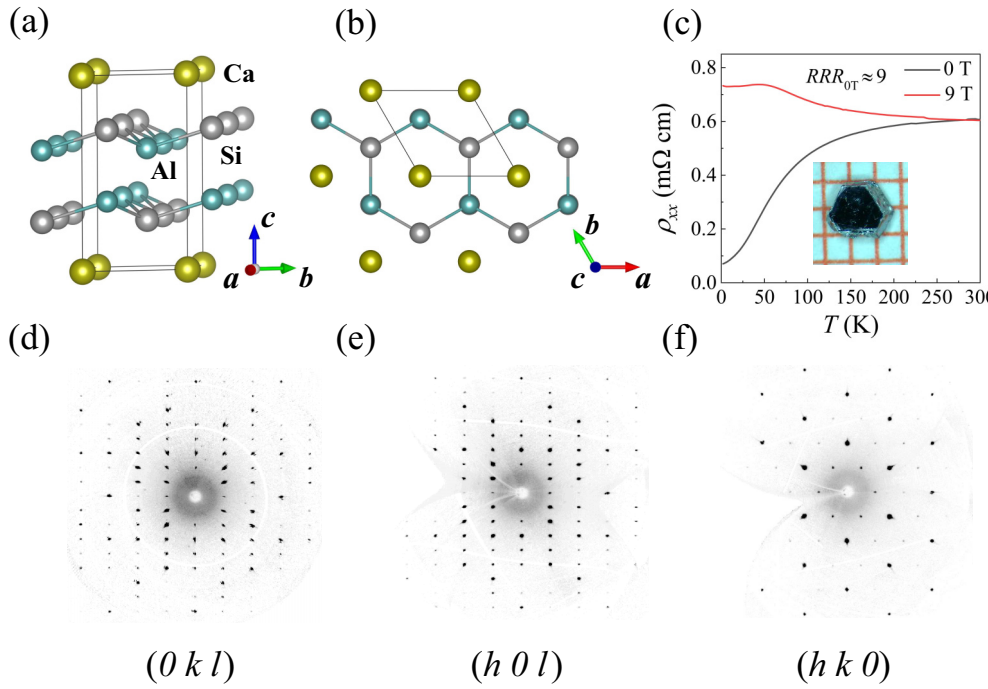

FIG. 1. (a),(b) Schematic crystal structure of $CaAl_2Si_2$ viewed along different orientations. (c) Temperature dependence of the longitudinal resistivity ρ_{xx}. Inset shows an image of a typical crystal. (d)–(f) Diffraction patterns in the reciprocal space along $(0kl)$, $(h0l)$, and $(hk0)$ directions.

is very difficult, and such materials are in fact very rare. Despite these difficulties, several materials were theoretically predicted to host multiple topological states, and some of them were even experimentally verified. In noncentrosymmetric cubic B20-type (space group: $P2_13$) CoSi, chiral crystal symmetry plays an essential role in protecting the unconventional multifold chiral fermions, i.e., the spin-1 chiral fermion carrying a Chern number $C = \pm 2$ with threefold band crossing and charge-2 DPs with fourfold degeneracy [19,20], as was proven by the very recent angle-resolve photoemission spectroscopy (ARPES) measurements [22,23]. In the layered transition-metal telluride $TaIrTe_4$, in addition to the well-separated WPs that were already predicted in k space above the Fermi level E_F, a pair of nodal lines protected by mirror symmetry was also detected by ARPES measurements [31]. These exciting experimental successes have greatly advanced our knowledge of band topology theory. In addition to CoSi and $TaIrTe_4$, other theoretically proposed candidates include C_4Li [32], the kagome compound Mg_3Bi_2 [33], and some polar hexagonal *ABC* crystals such as SrHgSn and CaHgSn [34], etc. The nonsymmorphic symmetries in the C_4Li protected nodal-line could coexist with the type-II DPs, while Mg_3Bi_2 hosts a type-II nodal-line with the protection of both TR and SI symmetries, and the spin-orbit coupling (SOC) could induce a pair of three-dimensional (3D) DPs that are independent of the nodal-line. In SrHgSn and CaHgSn, the crystal point symmetry, especially the sixfold rotation symmetry, protects a pair of band-inversion-generated DPs setting along the polar rotation axis. Simultaneously, six pairs of WPs that originated from inversion symmetry breaking caused by the HgPb layer bulking are in the plane perpendicular to the polar axis and are protected by the combined twofold rotation and TR symmetries. These predictions, however, are still waiting for experimental realization.

In this paper, we present studies by means of magnetotransport measurements and *ab initio* calculations on the layered $CaAl_2Si_2$ semimetal crystallized into the structure schematically depicted in Figs. 1(a) and 1(b) viewed along different orientations. The magnetotransport measurements reveal quantum oscillations of magnetoresistance (MR), which are closely related to the hole-1 Fermi pocket of the Fermi surface (FS) enclosing a nodal-line setting around the Γ point without the SOC. When the SOC is considered, the nodal-line is gapped and a pair of DPs protected by the C_3 symmetry appear along the Γ-A direction, which coexist with the SOC-induced topological insulator (TI) state along the same direction.

II. EXPERIMENT

$CaAl_2Si_2$ crystals were grown by using the self-flux method. Starting materials of Ca (99.95%, aladdin), Al (99.999%, aladdin), and Si (99.9999%, aladdin) blocks were mixed in a molar ratio of 1: 20: 2 and placed into an alumina crucible, which was then sealed into a quartz tube in vacuum. The assembly was heated in a furnace up to 1100 °C within 10 h, kept at that temperature for 20 h, and then slowly cooled down to 750 °C at a temperature-decreasing rate of 0.5 °C/h. The excess Al was removed at this temperature by quickly placing the assembly into a high-speed centrifuge, and black crystals with a shining surface in a typical dimension of $2.6 \times 2 \times 1.5\,mm^3$, shown in the inset of Fig. 1(c), were what was left.

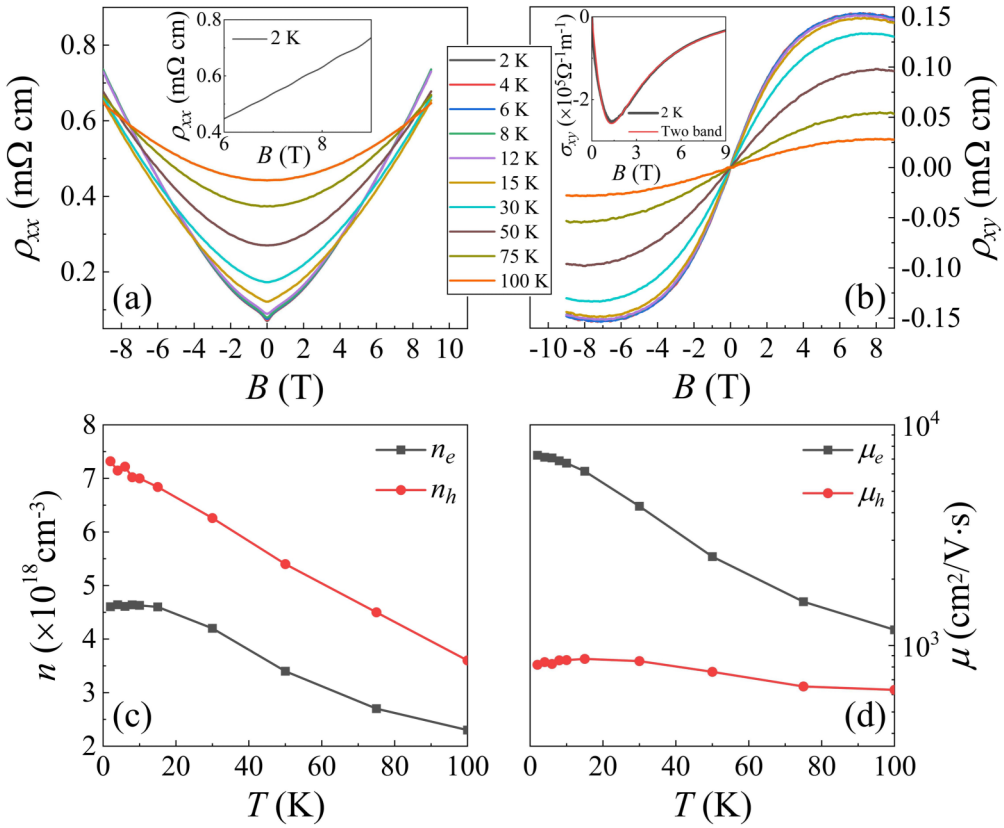

FIG. 2. (a) Longitudinal MR ρ_{xx} vs magnetic field B between $T = 2-100$ K. Inset enlarges the oscillations at 2 K. (b) Hall resistivity vs magnetic field B at different temperatures. Inset shows Hall conductivity at 2 K and the red line denotes the fitting by the two-band model. Parts (c),(d) show the temperature dependence of carrier densities and mobilities, respectively.

The phase and quality examinations of $CaAl_2Si_2$ were performed on a Bruker D8 single-crystal x-ray diffractometer (SXRD) with Mo $K\alpha 1$ ($\lambda = 0.710\,73$ Å) at 298 K. The diffraction pattern could be satisfyingly indexed on the basis of a trigonal structure with the lattice parameters $a = b = 4.137$ Å, $c = 7.131$ Å, $\alpha = \beta = 90^\circ$, and $\gamma = 120^\circ$ in the space group P-3m1 (No. 164), consistent with those reported earlier [35]. The perfect reciprocal space lattice without any other miscellaneous points, seen in Figs. 1(d)–1(f), indicates pure phase and high quality of the crystal used in this study. Paying close attention again to the schematic crystal structure in Fig. 1(a), which was drawn based on the refinement results from the SXRD data, we can find that the Al and Si atoms are arranged in double-corrugated hexagonal layers that are intercalated with Ca in such a way that a layered pile of $-Al_2Si_2-Ca-Al_2Si_2-$ is formed along the c-axis. The magnetotransport measurements, including the resistivity and Hall effect measurements, were carried out using a standard Hall bar geometry in a commercial DynaCool physical properties measurement system (PPMS) from Quantum Design. We used three crystals from the same batch for each of the resistivity, Hall effect, and magnetotransport measurements. The obtained data of the three crystals closely agree with each other, guaranteeing the reliability of the results.

The first-principles calculations were carried out within the framework of the projector augmented wave (PAW) method [36,37] and employed the generalized gradient approximation (GGA) [38] with the Perdew-Burke-Ernzerhof (PBE) formula [39], as implemented in the Vienna *ab initio* Simulation Package (VASP) [40–42]. A kinetic energy cutoff of 500 eV and a Γ-centered k mesh of $10 \times 10 \times 6$ were utilized in all the calculations. The energy and force difference criteria were defined as 10^{-6} eV and 0.01 eV/Å for self-consistent convergence and structural relaxation. The WANNIER90 package [43–45] was adopted to construct Wannier functions from the first-principles results without an iterative maximal-localization procedure. The WANNIERTOOLS [46] code was used to investigate the topological features of surface-state spectra.

III. RESULTS AND DISCUSSION

The temperature (T) dependence of longitudinal resistivity ρ_{xx} measured with B perpendicular to the (001) plane and the electrical current I along the b-axis at a magnetic field $B = 0$ T is presented in Fig. 1(c), which displays typical semimetallic conduction with a residual resistance ratio (RRR) $\rho_{xx}(300\text{ K})/\rho_{xx}(2\text{ K})$ of about 9. The application of $B = 9$ T significantly enhances ρ_{xx} to be somewhat insulating with a plateau behavior at low temperature, which is commonly observed in many topological semimetals [47–50]. Thermal evolution of the B-dependent ρ_{xx} measured in the temperature range of 2–100 K is summarized in Fig. 2(a) in the main panel.

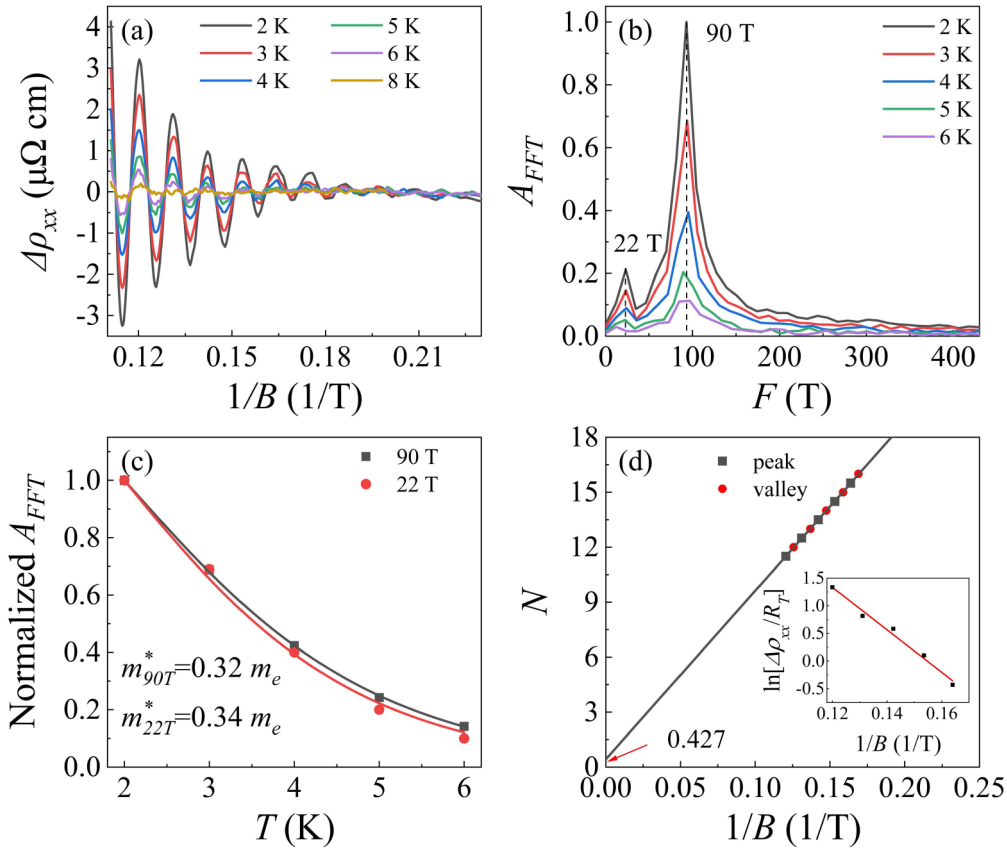

FIG. 3. (a) SdH oscillatory component as a function of $1/B$ after subtracting the sixth-order polynomial fit background. (b) FFT spectra of $\Delta\rho_{xx}$. (c) Temperature dependence of relative amplitudes of the FFT spectra for the fundamental frequencies of 22 T (red circle) and 90 T (black box). The solid lines denote the fitting by using the LK formula. (d) Landau-level indices extracted from the SdH oscillations plotted against $1/B$. The solid line denotes the linear plot to the data. Inset: Dingle plot of the SdH oscillation for 90 T at 2 K.

The MR, defined as MR $= [\rho(B) - \rho(0)]/\rho(0) \times 100\%$, in which $\rho(B)$ and $\rho(0)$ represent the resistivity with and without B, respectively, shows a crossover from a quadratic-like evolution to linear change, reaching $\sim 1000\%$ at 9 T and 2 K without showing any sign of saturation. Moreover, quantum oscillations in the MR can be observed at $B > 6$ T below 8 K, which could be seen more clearly by the enlarged view set as an inset in Fig. 2(a). This behavior had not been reported in earlier references [51]. The field dependence of Hall resistivity ρ_{xy} presented in Fig. 2(b) exhibits a clear deviation from the linear change at temperatures below 100 K, indicating that both electron and hole carriers participate in the transport. To quantitatively estimate the densities and mobilities of the carriers in $CaAl_2Si_2$, the Hall conductivity, i.e., $\sigma_{xy} = -\rho_{xy}/(\rho_{xy}^2 + \rho_{xx}^2)$, was fitted by employing the semiclassical two-band model [52,53]:

$$\sigma_{xy} = \left[\frac{n_h\mu_h^2}{1+(\mu_h B)^2} - \frac{n_e\mu_e^2}{1+(\mu_e B)^2}\right]eB,$$

where n_e (n_h) denotes the carrier density for the electron (hole), and μ_e (μ_h) is the mobility of the electron (hole). The fitting results at $T = 2$ K are presented by the inset of Fig. 2(b), unveiling that the two-band model could nicely describe the Hall conductivity. The fitting-yielded temperature dependences of densities and mobilities for electron and hole carriers are shown in Figs. 2(c) and 2(d), respectively. At 2 K, the carriers densities are $n_h = 7.32 \times 10^{18}$ cm^{-3} and $n_e = 4.6 \times 10^{18}$ cm^{-3}, revealing that the hole and electron carriers are in fact uncompensated, which could reasonably explain the smaller MR of $CaAl_2Si_2$ as compared with the extremely large MR in other compensated semimetals [54–56]. Though the densities for hole and electron carriers are at the same order of magnitude, the mobility of electron carries is about one order of magnitude larger than that of the hole carriers. Both n_h and μ_e decrease monotonically with decreasing temperature, whereas n_e is shown to be nearly temperature-independent below a temperature of 15 K and μ_h also reaches a maximal value around the same temperature. By using a similar equation, the fitting to σ_{xx} yielded rather similar results, as seen in the Supplementary Information (SI) [57].

To achieve a further understanding about the electronic band structure and map out the FS, quantum oscillations of the MR were analyzed in more detail. After carefully subtracting a sixth-order polynomial background, denoted by $\Delta\rho_{xx}$, striking Shubnikov–de Haas (SdH) oscillations are displayed. The SdH oscillations at different temperatures from 2 to 8 K against the reciprocal magnetic field $1/B$ are plotted in Fig. 3(a), which could be well described by the Lifshitz-Kosevich (LK) formula [58]

$$\Delta\rho \propto R_T R_D \cos\left[2\pi\left(\frac{F}{B} + \gamma - \delta + \varphi\right)\right],$$

TABLE I. Parameters derived from the SdH oscillations of $CaAl_2Si_2$.

F (T)	A (nm^{-2})	k_F (nm^{-1})	v_F (m/s)	m^*/m_e	T_D (K)	τ_Q (s)	μ (cm^2/Vs)	Berry phase
22	0.210	0.258	0.881×10^5	0.34				
90	0.857	0.522	1.893×10^5	0.32	8.078	1.506×10^{-13}	827.651	0.854π

where $R_T = 2\pi^2 k_B T/\hbar\omega_c/\sinh(2\pi^2 k_B T/\hbar\omega_c)$, $R_D = \exp(-2\pi^2 k_B T_D/\hbar\omega_c)$, k_B is the Boltzmann constant, $\hbar$ is Planck's constant, F is the oscillation's frequency, φ is the phase shift, $\omega_c = eB/m^*$ is the cyclotron frequency, with m^* denoting the effective cyclotron mass, and T_D is the Dingle temperature defined by $T_D = \hbar/2\pi k_B \tau_Q$, with τ_Q being the quantum scattering lifetime. The fast Fourier transform (FFT) spectra of the SdH oscillations, depicted in Fig. 3(b), disclose two fundamental frequencies at $F_1 = 22$ T and $F_2 = 90$ T. The corresponding external cross-sectional areas of the FS are $A = 0.210$ and $0.857\,\text{nm}^{-2}$, respectively, calculated by using the Onsager relation $F = (\hbar/2\pi e)A$. The effective cyclotron mass m^* at E_F could be obtained by fitting the temperature dependence of the FFT amplitude by the temperature damping factor of the LK equation expressed as R_T, as is shown in Fig. 3(c), giving $m^* = 0.34$ and $0.32m_e$, where m_e denotes the free-electron mass. The Fermi wave vectors are estimated to be 0.258 and $0.522\,\text{nm}^{-1}$ from $k_F = \sqrt{2eF/\hbar}$, and the very large Fermi velocities $v_F = 0.881 \times 10^5$ and $1.893 \times 10^5\,\text{m s}^{-1}$ are calculated from $v_F = \hbar k_F/m^*$. Because the frequency F_1 of 22 T is too small for the analysis of the Dingle temperature and quantum scattering lifetime, we only did the analysis on the frequency F_2 of 90 T, as seen by the inset of Fig. 3(d), giving $T_D = 8.078$ K and $\tau_Q = 1.5062 \times 10^{-13}$. Furthermore, the corresponding quantum mobility μ_Q ($= 827.651\,\text{cm}^2\,\text{V}^{-1}\text{s}^{-1}$) could also be obtained from the equation $\mu_Q = e\tau_Q/m^*$. The results are summarized in Table I.

Generally speaking, the pseudospin rotation under a magnetic field in a Dirac/Weyl system will produce a nontrivial φ_B that could be accessed from the Landau level (LL) index fan diagram or a direct fit to the SdH oscillations by using the LK formula. The phase shift is generally a sum expressed as $\gamma - \delta + \varphi$, where γ is the phase factor expressed as $1/2 - \varphi_B/2\pi$ and δ represents the dimension-dependent correction to the phase shift. In a two-dimensional (2D) case, δ amounts to zero, while in a 3D case δ is $\pm 1/8$, where the sign depends on the type of charge carriers and the kind of cross-section extremum. To provide more evidence for the nontrivial topological state in $CaAl_2Si_2$, the Berry phase φ_B was examined. Figure 3(d) shows the plot of the LL index N as a function of $1/B$ for the dominant frequency of $F_2 = 90$ T. Here the $\Delta\rho_{xx}$ valley positions (red circles) in $1/B$ were assigned to be integer indices, and the $\Delta\rho_{xx}$ peak positions (black boxes) were assigned to be half-integer indices. All of the points almost fall on a straight line, thus allowing a linear fitting that gives an intercept 0.427, which demonstrates a π Berry phase. This strongly indicates a nontrivial topological state in $CaAl_2Si_2$.

The angle-dependent MR is presented in Fig. 4(a), with the measurement geometry shown in the inset. The clear change in the angle-dependent magnitude of MR is probably due to the weakness of the Lorentz force. Figure 4(b) presents the angle-dependent SdH oscillations with a constant offset after subtracting the sixth-order polynomial background, which exhibits a clear shift of the peaks with the increase of θ, i.e., the angle between B and the c-axis. The θ dependence of fundamental frequencies derived from the SdH oscillations is shown in Fig. 4(c). The frequency F_2 changes from 90 T at $\theta = 0^\circ$ (out-of-plane) to 110 T at $\theta = 75^\circ$ (near the in-plane direction), unveiling the weak anisotropy of the Fermi pocket associated with the SdH oscillations.

To achieve in-depth insights into the SdH oscillations, the angular dependence of the FS cross-sectional areas according to the DFT calculations is shown in Fig. 4(e). There are four main sheets of FS, consisting of three hole pockets centered at the Γ point and one electron pocket centered at the M point of the BZ. The carrier concentrations in $CaAl_2Si_2$—$n_h = 5.71 \times 10^{18}\,\text{cm}^{-3}$ and $n_e = 4.22 \times 10^{18}\,\text{cm}^{-3}$—are estimated from the DFT calculations, which are in good agreement with those derived from the fitting to experimental data by using the two-band model. According to the calculation, the hole pockets marked as holes 2 and 3, and the electron pocket, can be excluded as the origin of the quantum oscillations because of the large mismatch in size between experiments and calculations. For the small hole 1 FS with a ring torus shape, the calculated frequencies for the in-plane case are 21 and 78 T, in good agreement with the experimental values. However, for the out-of-plane case there is a clear difference between the calculated and experimental values in that the calculated sizes are apparently larger than the experimental ones, as summarized in Table II and shown in Fig. 4(e), indicating that the areas of the Fermi pockets for the out-of-plane case are smaller than the calculated ones. The plot of LL index N as a function of $1/B$ of F_2 with varied angles presented in Fig. 4(d) indicates a nontrivial Berry phase. The result is summarized in Table III, which strongly demonstrates that the frequency of F_2 is derived from the hole 1 FS. This will be discussed below in more detail.

It is known that the quantum lifetime τ_Q of the holes is sensitive to all angle scattering processes that could broaden the Landau levels, while the transport lifetime τ_T is only susceptible to the large-angle scattering process. In principle, the τ_T/τ_Q ratio is a measure of the relative importance of small-angle scattering. According to the Hall effect measurement, the transport lifetime $\tau_T = m^*\mu_h/e = 1.488 \times 10^{-13}$ s, thus yielding the τ_T/τ_Q ratio of 0.988, indicating that the large-angle scattering plays a dominant role in the transport, which is different from the case in Cd_3As_2 [59].

The calculated band structure in the absence of SOC is shown in Fig. 5(a), indicating that $CaAl_2Si_2$ is a semimetal with an overlap between the valence and conduction bands. These results are in good agreement with previous electronic structure calculations and electrical resistivity measurements [35,51,60]. Note that the hole 1 FS with the ring torus shape is quite rare [61]. Along the Γ-K direction, there is a linear

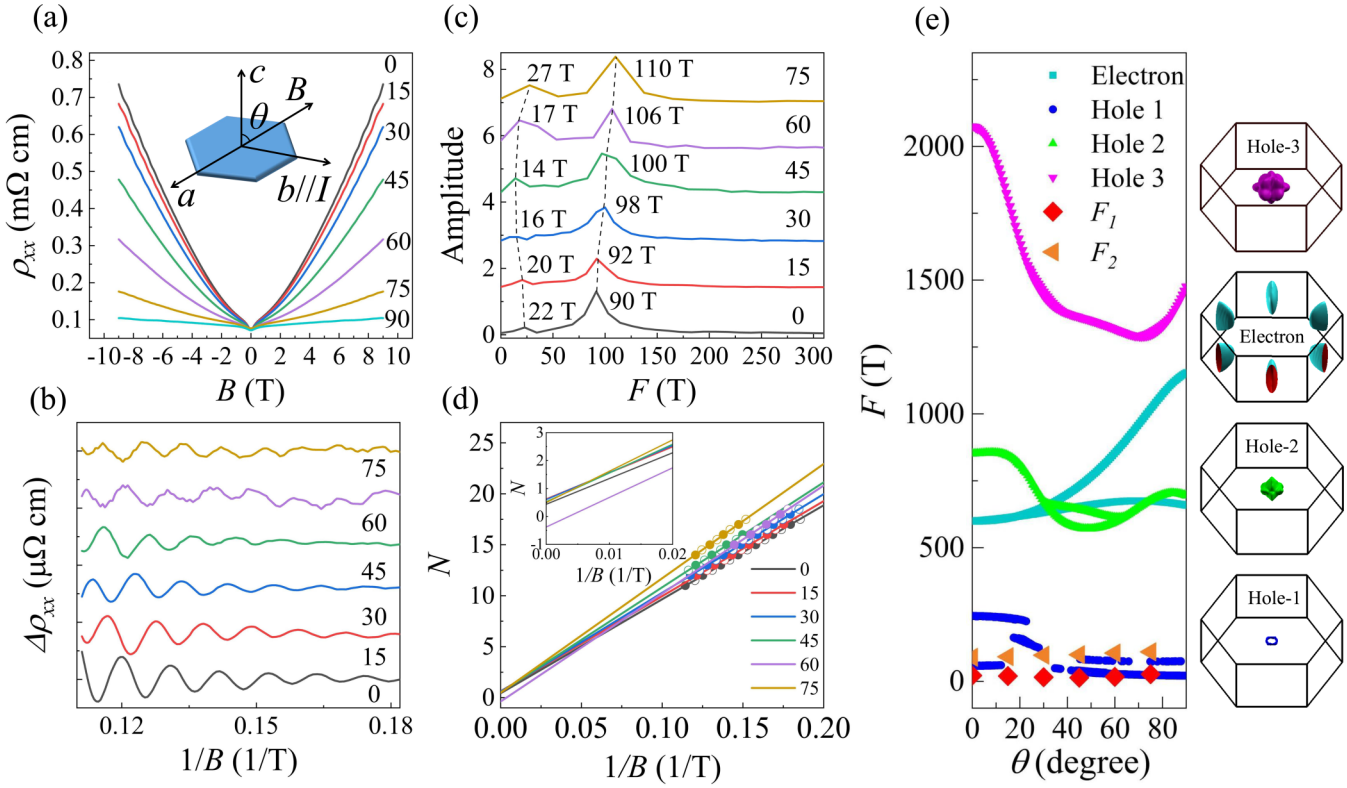

FIG. 4. (a) Longitudinal ρ_{xx} vs magnetic field B at different angles at 2 K. Inset shows the schematic measurement configuration. (b) SdH oscillatory component as a function of $1/B$ at different angles. (c) FFT spectra of $\Delta\rho_{xx}$ at different angles. (d) Plot of LL index N as a function of $1/B$ of F_2 at all angles. Inset: Enlarged view for the fitted intercepts. (e) Quantum oscillation frequencies as a function of the angle θ for the four FSs compared between experimental and calculated values. Right picture shows the shapes of the four FSs of $CaAl_2Si_2$.

band crossing near the E_F, as seen in Fig. 5(b), whereas there is a tiny band gap along the Γ-M direction. The band crossing structure is confirmed by additional hybrid functional calculations in the Heyd-Scuseria-Ernzerhof (HSE06) scheme. Fat band analysis, seen in the SI [57], shows that there is a band inversion between Al-s and Si-p_{xy} orbitals at the Γ point, suggesting nontrivial band topology of $CaAl_2Si_2$. Due to the presence of both TR and SI symmetries, the spinless Hamiltonian is completely real-valued [33,62]. The band crossing as such does not appear by itself but actually persists along a closed path around the Γ point, as schematically plotted in Fig. 5(c). Because of the absence of protection from mirror reflection, glide plane, or screw axes symmetries, the nodal-line in $CaAl_2Si_2$ does not exactly lie on the $k_z = 0$ plane and is fragile to the SOC [63]. Figure 5(d) shows the surface spectrum for the semi-infinite (001) surface, in which the nontrivial drumhead-like surface states, indicated by white arrows in the inset of Fig. 5(d), dispersing outward from the nodal-line, are clearly observed. When SOC is considered, the nodal-line enclosed by hole 1 FS in $CaAl_2Si_2$ is gapped, as shown in Fig. 5(e).

Another effect of SOC is that it produces a symmetry-protected linear band crossing between the bands with Δ_4 and Δ_{5+6} irreducible representations (IRs) along the Γ-A direction, as shown in Figs. 6(a) and 6(b). The band crossing is fourfold degenerate and protected by the C_3 rotation symmetry, forming a pair of Dirac points located at BZ coordinates $(0, 0, k_z^D \approx \pm 0.278 \times \frac{2\pi}{c})$ and an energy of $E -$

TABLE II. A comparison of the calculated and experimental fundamental frequencies and effective mass of the Fermi pockets for the in-plane and out-of-plane cases, respectively.

	Hole-1		Hole-2		Hole-3		Electron		Experiment	
	F (T)	$m^*(m_e)$	F (T)	$m^*(m_e)$	F (T)	$m^*(m_e)$	F (T)	$m^*(m_e)$	F (T)	$m^*(m_e)$
In-plane	21	0.11	695	0.46	1475	0.76	659	0.36	~27	
	78	0.24					1153	0.62	~110	
Out-of-plane	57	0.18	851	0.5	2075	1	600	0.32	22	0.34
	245	0.22							90	0.32

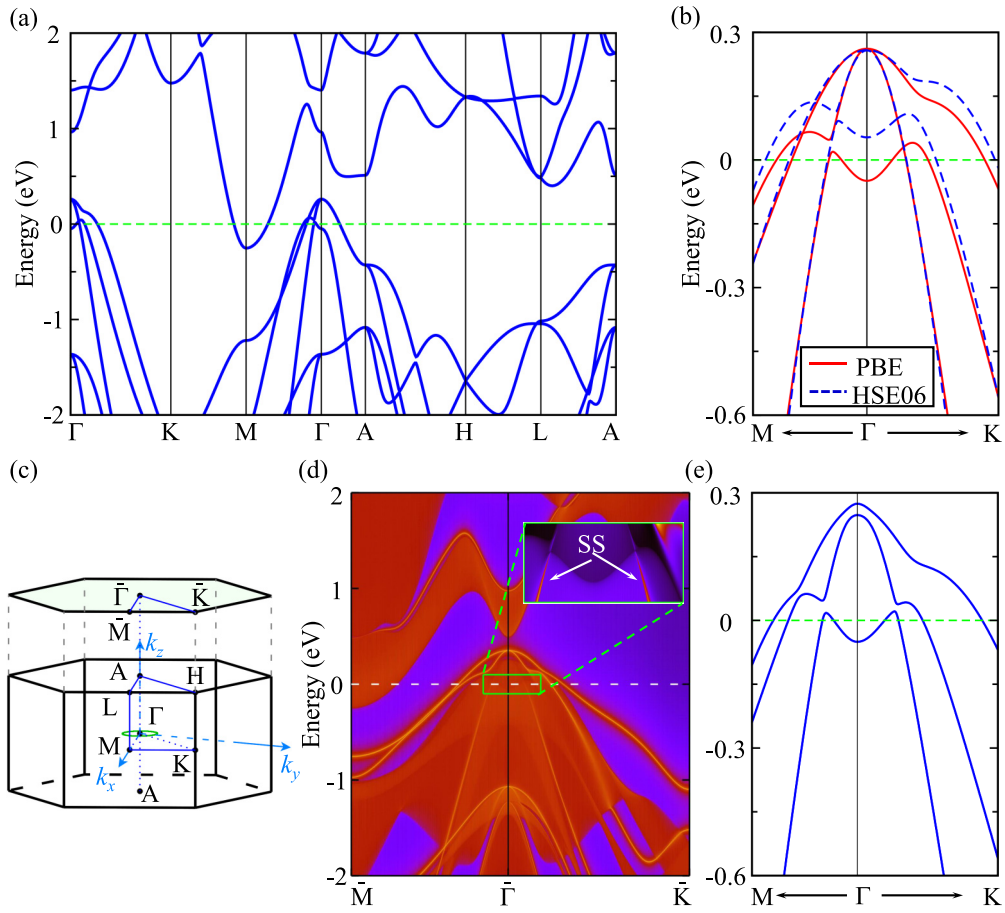

FIG. 5. (a) Electronic band structure of $CaAl_2Si_2$ without including SOC. (b) Enlarged band structure along Γ-*M* and Γ-*K* paths calculated at PBE and HSE06 levels of theory. (c) Bulk BZ, (001) projected surface BZ, and high-symmetry points. The nodal line inside the BZ is illustrated in green. (d) Surface band structure of $CaAl_2Si_2$ on the (001) projected surface. The inset shows the zoom-in view of the solid green box area, where the nontrivial topological surface states situated outside the projected nodal line are pointed out by white arrows and are clearly visible. (e) Electronic band structure $CaAl_2Si_2$ with including SOC.

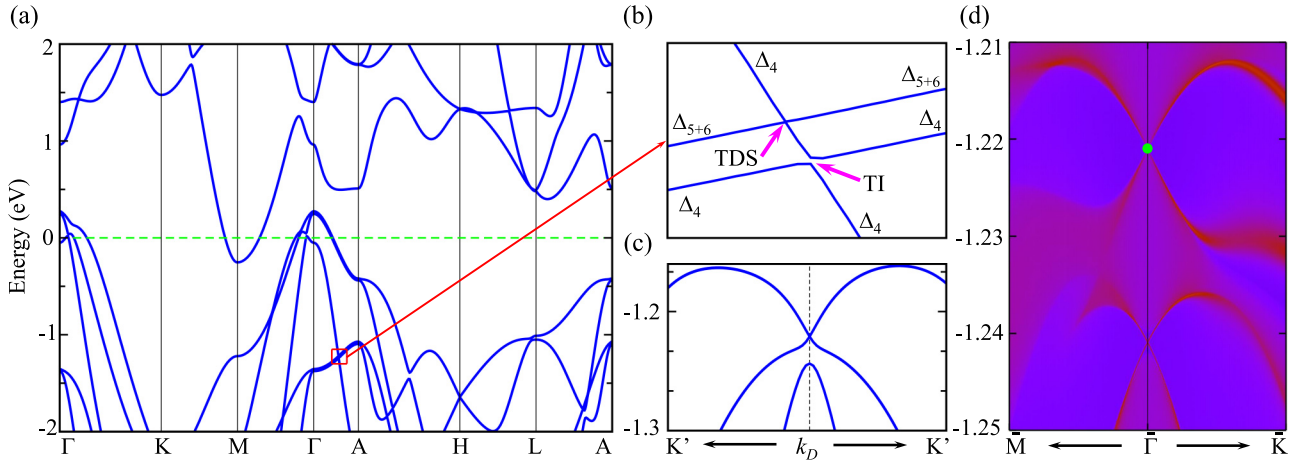

FIG. 6. (a) Electronic band structure of $CaAl_2Si_2$ with considering SOC. (b) Enlarged view of the solid red area in (a). The irreducible representations of selected bands along the high symmetric *k* are indicated. (c) Electronic band structure in the k_x-k_y plane surrounding the Dirac point. (c) The (001) surface band structure of $CaAl_2Si_2$ in the presence of SOC.

TABLE III. Berry phase for the fundamental frequency F_2 with varied angles between the magnetic field and current.

θ	0	15	30	45	60	75
Berry phase	0.854π	1.2π	1.2π	1.04π	-0.76π	0.99π

$E_F = -1.22$ eV. Note that the band crossing is titled along the Γ-*A* direction, while it is straight perpendicular to the Γ-*K* direction, as seen in Fig. 6(c). In addition to DSM states, SOC also induces a hybridization between two Δ_4 bands and opens a gap of about 3 meV, leading to a TI state, resembling that of Fe(Te,Se) [64] and LiFeAs [65], which indicates multiple topological states in $CaAl_2Si_2$. For both DSM and TI states, nontrivial topological surface states should exist. The calculated surface states on the (001) surface are illustrated in Fig. 6(d) to further confirm the topological nature of $CaAl_2Si_2$. For the TI state, the surface shows protected nontrivial Dirac cone type topological surface states inside the SOC gap at the Γ point. For the DSM state, the surface exhibits a gapless linear-dispersion bulk state and a linear Dirac cone surface state.

The nontrivial topological states in $CaAl_2Si_2$ naturally call to mind the isostructural topological semimetals $EuCd_2As_2$ and $EuCd_2Sb_2$ [66–69], which belong to the type IV magnetic space group. They were initially proposed to host DSM states, whereas the latter experiments revealed that the peculiar *A*-type antiferromagnetic structure could break the C_3 symmetry along the *c*-axis, and the DP near E_F along the Γ-*Z* path of BZ is no longer protected by the combined inversion and nonsymmorphic time-reversal symmetries, but rather opens tiny band gaps, making the two compounds topological insulators rather than DSMs [70]. In $CaAl_2Si_2$, the absence of magnetism could well preserve the C_3 symmetry and hence the DSM state, thus highlighting again the necessary role of certain symmetries in protecting nontrivial topological states.

IV. SUMMARY

In conclusion, the peculiar hole 1 Fermi pocket in the band structure of layered $CaAl_2Si_2$ plays a decisive role in dominating the magnetotransport properties. The nontrivial Berry phase unveiled that $CaAl_2Si_2$ is a topological semimetal hosting a nodal-line close to the Fermi level in the absence of SOC. Once the SOC is taken into account, the topological nodal-line will be gapped, and a pair of Dirac points, together with the SOC-induced topological state, will emerge along the highly symmetric Γ-*A* direction. These intriguing multiple nontrivial topological states make $CaAl_2Si_2$ an excellent platform for the study of novel topological physics.

ACKNOWLEDGMENTS

The authors acknowledge the support by the Natural Science Foundation of Shanghai (Grant No. 17ZR1443300) and the National Natural Science Foundation of China (Grant No. 11874264). Y.F.G. acknowledges the starting grant of ShanghaiTech University and the Program for Professor of Special Appointment (Shanghai Eastern Scholar) and the strategic Priority Research Program of Chinese Academy of Sciences (Grant No. XDA18000000). W.Z. is supported by the Shenzhen Peacock Team Plan (Grant No. KQTD20170809110344233), and Bureau of Industry and Information Technology of Shenzhen through the Graphene Manufacturing Innovation Center (Grant No. 201901161514). G.X. acknowledges support from the National Key Research and Development Program of China (Grant No. 2018YFA0307000) and the National Natural Science Foundation of China (Grant No. 11874022). The authors gratefully acknowledge the support from Analytical Instrumentation Center (No. SPST-AIC10112914), SPST, ShanghaiTech University.

H. S. and X. S. contributed equally to this work.

[1] X. Wan, A. M. Turner, A. Vishwanath, and S. Y. Savrasov, Phys. Rev. B **83**, 205101 (2011).

[2] Z. Wang, Y. Sun, X.-Q. Chen, C. Franchini, G. Xu, H. Weng, X. Dai, and Z. Fang, Phys. Rev. B **85**, 195320 (2012).

[3] A. A. Burkov, M. D. Hook, and L. Balents, Phys. Rev. B **84**, 235126 (2011).

[4] H. Weng, X. Dai, and Z. Fang, J. Phys.: Condens. Matter **28**, 303001 (2016).

[5] S. M. Young, S. Zaheer, J. C. Y. Teo, C. L. Kane, E. J. Mele, and A. M. Rappe, Phys. Rev. Lett. **108**, 140405 (2012).

[6] Z. Wang, H. Weng, Q. Wu, X. Dai, and Z. Fang, Phys. Rev. B **88**, 125427 (2013).

[7] Z. K. Liu, J. Jiang, B. Zhou, Z. J. Wang, Y. Zhang, H. M. Weng, D. Prabhakaran, S.-K. Mo, H. Peng, P. Dudin, T. Kim, M. Hoesch, Z. Fang, X. Dai, Z. X. Shen, D. L. Feng, Z. Hussain, and Y. L. Chen, Nat. Mater. **13**, 677 (2014).

[8] Z. K. Liu, B. Zhou, Y. Zhang, Z. J. Wang, H. M. Weng, D. Prabhakaran, S.-K. Mo, Z. X. Shen, Z. Fang, X. Dai, Z. Hussain, and Y. L. Chen, Science **343**, 864 (2014).

[9] B. Q. Lv, H. M. Weng, B. B. Fu, X. P. Wang, H. Miao, J. Ma, P. Richard, X. C. Huang, L. X. Zhao, G. F. Chen, Z. Fang, X. Dai, T. Qian, and H. Ding, Phys. Rev. X **5**, 031013 (2015).

[10] S.-Y. Xu, I. Belopolski, N. Alidoust, M. Neupane, G. Bian, C. L. Zhang, R. Sankar, G. Q. Chang, Z. J. Yuan, C.-C Lee, S.-M. Huang, H. Zheng, J. Ma, D. S. Sanchez, B. K. Wang, A. Bansil, F. C. Chou, P. P. Shibayev, H. Lin, S. Jia, and M. Z. Hasan, Science **349**, 613 (2015).

[11] G. Chang, S.-Y. Xu, B. J. Wieder, D. S. Sanchez, S.-M. Huang, I. Belopolski, T.-R. Chang, S. Zhang, A. Bansil, H. Lin, and M. Z. Hasan, Phys. Rev. Lett. **119**, 206401 (2017).

[12] H. Weng, C. Fang, Z. Fang, B. A. Bernevig, and X. Dai, Phys. Rev. X **5**, 011029 (2015).

[13] K. Deng, G. L. Wan, P. Deng, K. N. Zhang, S. J. Ding, E. Y. Wang, M. Z. Yan, H. Q. Huang, H. Y. Zhang, Z. L. Xu, J. Denlinger, A. Fedorov, H. T. Yang, W. H. Duan, H. Yao, Y. Wu, S. S. Fan, H. J. Zhang, X. Chen, and S. Y. Zhou, Nat. Phys. **12**, 1105 (2016).

[14] L. Huang, T. M. McCormick, M. Ochi, Z. Y. Zhao, M. Suzuki, R. Arita, Y. Wu, D. X. Mou, H. B. Cao, J. Q. Yan, N. Trivedi, and A. Kaminski, Nat. Mater. **15**, 1155 (2016).

[15] L. X. Yang, Z. K. Liu, Y. Sun, H. Peng, H. F. Yang, T. Zhang, B. Zhou, Y. Zhang, Y. F. Guo, M. Rahn, D. Prabhakaran, Z. Hussain, S.-K. Mo, C. Felser, B. Yan, and Y. L. Chen, Nat. Phys. **11**, 728 (2015).

[16] Z. K. Liu, L. X. Yang, Y. Sun, T. Zhang, H. Peng, H. F. Yang, C. Chen, Y. Zhang, Y. F. Guo, D. Prabhakaran, M. Schmidt, Z. Hussain, S.-K. Mo, C. Felser, B. Yan, and Y. L. Chen, Nat. Mater. **15**, 27 (2016).

[17] L. Fu and C. L. Kane, Phys. Rev. Lett. **100**, 096407 (2008).

[18] E. Tang and L. Fu, Nat. Phys. **10**, 964 (2014).

[19] B. Bradlyn, J. Cano, Z. J. Wang, M. G. Vergniory, C. Felser, R. J. Cava, and B. A. Bernevig, Science **353**, aaf5037 (2016).

[20] P. Tang, Q. Zhou, and S.-C. Zhang, Phys. Rev. Lett. **119**, 206402 (2017).

[21] J. Z. Ma, C. J. Yi, B. Q. Lv, Z. J. Wang, S. M. Nie, L. Wang, L. Y. Kong, Y. B. Huang, P. Richard, P. Zhang, K. Yaji, K. Kuroda, S. Shin, H. M. Weng, B. A. Bernevig, Y. G. Shi, T. Qian, and H. Ding, Sci. Adv. **3**, e1602415 (2017).

[22] Z. C. Rao, H. Li, T. T. Zhang, S. J. Tian, C. H. Li, B. B. Fu, C. Y. Tang, L. Wang, Z. L. Li, W. H. Fan, J. J. Li, Y. B. Huang, Z. H. Liu, Y. W. Long, C. Fang, H. M. Weng, Y. G. Shi, H. C. Lei, T. Qian, and H. Ding, Nature (London) **567**, 496 (2019).

[23] D. Takane, Z. W. Wang, S. Souma, K. Nakayama, T. Nakamura, H. Oinuma, Y. Nakata, H. Iwasawa, C. Cacho, T. Kim, K. Horiba, H. Kumigashira, T. Takahashi, Y. Ando, and T. Sato, Phys. Rev. Lett. **122**, 076402 (2019).

[24] A. A. Soluyanov, D. Gresch, Z. Wang, Q. Wu, M. Troyer, X. Dai, and B. A. Bernevig, Nature (London) **527**, 495 (2015).

[25] S. Y. Xu, N. Alidoust, G. Q. Chang, H. Lu, B. Singh, I. Belopolski, D. S. Sanchez, X. Zhang, G. Bian, H. Zheng, M. A. Husanu, Y. Bian, S. M. Huang, C. H. Hsu, T. R. Chang, H. T. Jeng, A. Bansil, T. Neupert, V. N. Strocov, H. Lin, S. A. Jia, and M. Z. Hasan, Sci. Adv. **3**, e1603266 (2017).

[26] M. Z. Yan, H. Q. Huang, K. N. Zheng, E. Y. Wang, W. Yao, K. Deng, G. L. Wan, H. Y. Zhang, M. Rrita, H. T. Yang, Z. Sun, H. Yao, Y. Wu, S. S. Fan, W. H. Duan, and S. Y. Zhou, Nat. Commun. **8**, 257 (2017).

[27] T. R. Chang, S. Y. Xu, D. S. Sanchez, W. F. Tsai, S. M. Huang, G. Q. Chang, C. H. Hsu, G. Bian, I. Belopolski, Z. M. Yu, S. Y. A. Yang, T. Neupert, H. T. Jeng, H. Lin, and M. Z. Hasan, Phys. Rev. Lett. **119**, 026404 (2017).

[28] T. E. O'Brien, M. Diez, and C. W. J. Beenakker, Phys. Rev. Lett. **116**, 236401 (2016).

[29] M. N. Ali, J. Xiong, S. Flynn, J. Tao, Q. D. Gibson, L. M. Schoop, T. Liang, N. Haldolaarachchige, N. P. Ong, and R. J. Cava, Nature (London) **514**, 205 (2014).

[30] M. Udagawa and E. J. Bergholtz, Phys. Rev. Lett. **117**, 086401 (2016).

[31] X. Q. Zhou, Q. H. Liu, Q. S. Wu, T. Nummy, H. X. Li, J. Griffith, S. Parham, J. Waugh, E. Emmanouilidou, B. Shen, O. V. Yazyev, N. Ni, and D. Dessau, Phys. Rev. B **97**, 241102(R) (2018).

[32] A. S. Cuamba, P. Hosur, H.-Y. Lu, L. Hao, and C. S. Ting, Phys. Rev. B **96**, 195159 (2017).

[33] X. M. Zhang, L. Jin, X. F. Dai, and G. D. Liu, J. Phys. Chem. Lett. **8**, 4814 (2017).

[34] H. Gao, Y. Kim, J. W. F. Venderbos, C. L. Kane, E. J. Mele, A. M. Rappe, and W. Ren, Phys. Rev. Lett. **121**, 106404 (2018).

[35] M. Imai, H. Abe, and K. Yamada, Inorg. Chem. **43**, 5186 (2004).

[36] P. E. Blöchl, Phys. Rev. B **50**, 17953 (1994).

[37] J. Lehtomäki, I. Makkonen, M. A. Caro, and O. J. Lopez-Acevedo, J. Chem. Phys. **141**, 234102 (2014).

[38] J. P. Perdew and Y. Wang, Phys. Rev. B **45**, 13244 (1992).

[39] J. P. Perdew, K. Burke, and M. Ernzerhof, Phys. Rev. Lett. **77**, 3865 (1996).

[40] G. Kresse and J. Hafner, Phys. Rev. B **47**, 558 (1993).

[41] G. Kresse and J. Furthmüller, Comput. Mater. Sci. **6**, 15 (1996).

[42] G. Kresse and J. Furthmüller, Phys. Rev. B **54**, 11169 (1996).

[43] A. A. Mosto, J. R. Yates, Y.-S. Lee, I. Souza, D. Vanderbilt, and N. Marzari, Comput. Phys. Commun. **178**, 685 (2008).

[44] N. Marzari and D. Vanderbilt, Phys. Rev. B **56**, 12847 (1997).

[45] I. Souza, N. Marzari, and D. Vanderbilt, Phys. Rev. B **65**, 035109 (2001).

[46] Q. S. Wu, S. N. Zhang, H. F. Song, M. Troyer, and A. A. Soluyanov, Comput. Phys. Commun. **224**, 405 (2018).

[47] W. Gao, N. Hao, F.-W. Zheng, W. Ning, M. Wu, X. Zhu, G. Zheng, J. Zhang, J. Lu, H. Zhang, C. Xi, J. Yang, H. Du, P. Zhang, Y. Zhang, and M. Tian, Phys. Rev. Lett. **118**, 256601 (2017).

[48] H. Y. Wang, H. Su, J. Y. Zhang, W. Xia, Y. S. Lin, X. L. Liu, X. F. Hou, Z. H. Yu, N. Yu, X. Wang, Z. Q. Zou, Y. H. Wang, Q. F. Liang, Y. H. Zhen, and Y. F. Guo, Phys. Rev. B **100**, 115127 (2019).

[49] Y. L. Wang, L. R. Thoutam, Z. L. Xiao, J. Hu, S. Das, Z. Q. Mao, J. Wei, R. Divan, A. Luican-Mayer, and G. W. Crabtree *et al.*, Phys. Rev. B **92**, 180402(R) (2015).

[50] Y.-Y. Wang, Q.-H. Yu, P.-J. Guo, K. Liu, and T.-L. Xia, Phys. Rev. B **94**, 041103(R) (2016).

[51] D. G. Costa, R. B. Capaz, R. Falconi, S. Strikos, and M. El Massalami, Sci. Rep. **8**, 4102 (2018).

[52] L. X. Zhao, L. C. Xu, H. K. Zuo, X. M. Wu, G. Y. Gao, and Z. W. Zhu, Phys. Rev. B **98**, 085137 (2018).

[53] A. B. Pippard, *Magnetoresistance in Metals* (Cambridge University Press, Cambridge, 1989).

[54] E. Emmanouilidou, B. Shen, X. Deng, T.-R. Chang, A. Shi, G. Kotliar, S.-Y. Xu, and N. Ni, Phys. Rev. B **95**, 245113 (2017).

[55] Z. Yuan, H. Lu, Y. Liu, J. Wang, and S. Jia, Phys. Rev. B **93**, 184405 (2016).

[56] D. S. Wu, J. Liao, W. Yi, X. Wang, P. G. Li, H. M. Weng, Y. G. Shi, Y. Q. Li, J. L. Luo, X. Dai, and Z. Fang, Appl. Phys. Lett. **108**, 042105 (2016).

[57] See Supplemental Material at http://link.aps.org/supplemental/10.1103/PhysRevB.101.205138 for the fitting to the longitudinal conductivity with the two-carrier model, the comparison of the fitting results with those obtained by fitting the Hall conductivity, and the fat band calculation.

[58] E. M. Lifshits and A. M. Kosevich, J. Phys. Chem. Solids **4**, 1 (1958).

[59] T. Liang, Q. Gibson, M. N. Ali, M. Liu, R. J. Cava, and N. P. Ong, Nat. Mater. **14**, 280 (2014).

[60] G. Q. Huang, M. Liu, L. F. Chen, and D. Y. Xing, J. Phys.: Condens. Matter **17**, 7151 (2005).

[61] D. Takane, K. Nakayama, S. Souma, T. Wada, Y. Okamotom, K. Takenaka, Y. Yamakawa, A. Yamakage, T. Mitsuhashi,

K. Horiba, H. Kumigashira, T. Takahashi, and T. Sato, npj Quantum Mater. **3**, 1 (2018).

[62] H. Weng, Y. Liang, Q. Xu, R. Yu, Z. Fang, X. Dai, and Y. Kawazoe, Phys. Rev. B **92**, 045108 (2015).

[63] C. Fang, Y. Chen, H.-Y. Kee, and L. Fu, Phys. Rev. B **92**, 081201(R) (2015).

[64] P. Zhang, K. Yaji, T. Hashimoto, Y. Ota, T. Kondo, K. Okazaki, Z. Wang, J. Wen, G. D. Gu, H. Ding, and S. Shin, Science **360**, 182 (2018).

[65] P. Zhang, Z. Wang, X. Wu, K. Yaji, Y. Lshida, Y. Kohama, G. Dai, Y. Sun, C. Bareille, K. Kuroda, T. Kondo, K. Okazaki, K. Kindo, X. Wang, C. Jin, J. Hu, R. Thomale, K. Sumida, S. Wu, K. Miyamoto, T. Okuda, H. Ding, G. D. Gu, T. Tamegai, T. Kawakami, M. Sato, and S. Shin, Nat. Phys. **15**, 41 (2019).

[66] L.-L. Wang, N. H. Jo, B. Kuthanazhi, Y. Wu, R. J. McQueeney, A. Kaminski, and P. C. Canfield, Phys. Rev. B **99**, 245147 (2019).

[67] J.-Z. Ma, S. M. Nie, C. J. Yi, J. Jandke, T. Shang, M. Y. Yao, M. Naamneh, L. Q. Yan, Y. Sun, A. Chikina, V. N. Strocov, M. Medarde, M. Song, Y.-M. Xiong, G. Xu, W. Wulfhekel, J. Mesot, M. Reticcioli, C. Franchini, C. Mudry, M. Müller, Y. G. Shi, T. Qian, H. Ding, and M. Shi, Sci. Adv. **5**, eaaw4718 (2019).

[68] J.-R. Soh, F. de Juan, M. G. Vergniory, N. B. M. Schröter, M. C. Rahn, D. Y. Yan, J. Jiang, M. Bristow, P. A. Reiss, J. N. Blandy, Y. F. Guo, Y. G. Shi, T. K. Kim, A. McCollam, S. H. Simon, Y. Chen, A. I. Coldea, and A. T. Boothroyd, Phys. Rev. B **100**, 201102(R) (2019).

[69] H. Su, B. C. Gong, W. J. Shi, H. F. Yang, H. Y. Wang, W. Xia, Z. H. Yu, P.-J. Guo, J. H. Wang, L. C. Ding, L. C. Xu, X. K. Li, X. Wang, Z. Q. Zou, N. Yu, Z. W. Zhu, Y. L. Chen, Z. K. Liu, K. Liu, G. Li, and Y. F. Guo, APL Mater. **8**, 011109 (2020).

[70] M. C. Rahn, J.-R. Soh, S. Francoual, L. S. I. Veiga, J. Strempfer, J. Mardegan, D. Y. Yan, Y. F. Guo, Y. G. Shi, and A. T. Boothroyd, Phys. Rev. B **97**, 214422 (2018).